JAAS

PAPER

View Article Online
View Journal | View Issue

Cite this: *J. Anal. At. Spectrom.*, 2015, **30**, 613

Full spectral XANES imaging using the Maia detector array as a new tool for the study of the alteration process of chrome yellow pigments in paintings by Vincent van Gogh†

Letizia Monico,*[ab] Koen Janssens,[b] Matthias Alfeld,[c] Marine Cotte,[de] Frederik Vanmeert,[b] Chris G. Ryan,[f] Gerald Falkenberg,[c] Daryl L. Howard,[g] Brunetto Giovanni Brunetti[a] and Costanza Miliani[a]

A combination of synchrotron radiation (SR) micro X-ray fluorescence (μ-XRF) and XRF mode X-ray absorption near edge structure (XANES) measurements at the Cr K-edge already allowed us to establish that the photo-reduction of chromates to Cr(III) compounds is the cause of darkening of chrome yellow pigments ($PbCr_{1-x}S_xO_4$, $0 \leq x \leq 0.8$) in a number of paintings by Vincent van Gogh and in corresponding artificially aged paint models. A silicon drift detector (SDD) was employed to record the Cr-K XRF radiation in these X-ray micro beam-based measurements. However, in view of the limited count rate capabilities and collection solid angle of a single device, μ-XRF and μ-XANES employing single element SDDs (or similar) are primarily suited for collection of spectral data from individual points. Additionally, collection of XRF maps *via* point-by-point scanning with relatively long dwell times per point is possible but is usually confined to small areas. The development of the 384 silicon-diode array Maia XRF detector has provided valuable solutions in terms of data acquisition rate, allowing for full spectral (FS) XANES imaging in XRF mode, *i.e.*, where spectroscopic information is available at each pixel in the scanned map. In this paper, the possibilities of SR Cr K-edge FS-XANES imaging in XRF mode using the Maia detector are examined as a new data collection strategy to study the speciation and distribution of alteration products of lead chromate-based pigments in painting materials. The results collected from two micro-samples taken from two Van Gogh paintings and an aged paint model show the possibility to perform FS-XANES imaging in practical time frames (from several minutes to a few hours) by scanning regions of sample sizes of the same order (more than 500 μm). The sensitivity and capabilities of FS-XANES imaging in providing representative chemical speciation information at the microscale (spatial resolution from ~2 to 0.6 μm) over the entire scanned area are demonstrated by the identification of $Cr(OH)_3$, Cr(III) sulfates and/or Cr(III) organometallic compounds in the corresponding phase maps, as alteration products. Comparable Cr-speciation results were obtained by performing equivalent higher spatial resolution SR μ-XRF/single-point μ-XANES analysis using a more conventional SDD from smaller regions of interest of each sample. Thus, large-area XRF mode FS-XANES imaging (Maia detector) is here proposed as a valuable and complementary data collection strategy in relation to "zoomed-in" high-resolution μ-XRF mapping and single-point μ-XANES analysis (SDD).

Received 12th November 2014
Accepted 17th December 2014

DOI: 10.1039/c4ja00419a

www.rsc.org/jaas

[a]*National Research Council-Insitute of Molecular Science and Technologies (CNR-ISTM) and Centre SMAArt, c/o Department of Chemistry, Biology and Biotechnologies, University of Perugia, via Elce di Sotto 8, 06123 Perugia, Italy. E-mail: letizia.monico@uantwerpen.be*

[b]*University of Antwerp, Department of Chemistry, Groenenborgerlaan 171, 2020 Antwerp, Belgium*

[c]*Deutsches Elektronen-Synchrotron, Notkestraße 85, 22603 Hamburg, Germany*

[d]*European Synchrotron Radiation Facility, Avenue des Martyrs 71, 38000 Grenoble, France*

[e]*Laboratoire d'Archéologie Moléculaire et Structurale, CNRS-UPMC, UMR 8220, place Jussieu 4, 75005 Paris, France*

[f]*Commonwealth Scientific and Industrial Research Organisation, Minerals Research Flagship, Normanby Road, Clayton, Victoria 3168, Australia*

[g]*Australian Synchrotron, 800 Blackburn Road, Clayton, Victoria 3168, Australia*

† Electronic supplementary information (ESI) available. See DOI: 10.1039/c4ja00419a

1. Introduction

During the last few decades, synchrotron radiation (SR)-based X-ray microprobe techniques, such as micro X-ray fluorescence (μ-XRF) and X-ray absorption near edge structure (XANES) methods (in point analysis or in mapping mode), have been successfully employed for the study of the degradation pathways of artists' pigments due to their valuable capabilities to provide information on the speciation and on the distribution of secondary compounds from the micrometer- to nanometer-scale.[1–3]

In many cases, the chromatic alteration encountered in specific areas of paintings from antiquity to the late 18th century can be ascribed to redox processes and/or modification of metal coordination of some inorganic compounds, such as the pigments cinnabar (HgS),[4,5] smalt (a potash glass in which the color stems from cobalt ions),[6,7] Prussian blue ($MFe^{III}[Fe^{II}(CN)_6]\cdot xH_2O$, with M = K^+, NH_4^+ or Na^+),[8,9] copper resinate[10] and verdigris[11] (both green copper organometallic compounds). Regarding late 19th–early 20th century yellow pigments, the photo-oxidation of the original CdS (cadmium yellow) to $CdSO_4$ was proposed as the mechanism responsible for fading of some yellow areas in masterpieces by Ensor,[12] Van Gogh[13] and Matisse,[14] whereas the photo-reduction of the zinc yellow pigment ($K_2O\cdot 4ZnCrO_4\cdot 3H_2O$) to ochre-green Cr(III) compounds was identified as a cause of the chromatic alteration in a painting by Seurat.[15] A light-induced reduction is also the cause of darkening in selected chrome yellow paint areas ($PbCr_{1-x}S_xO_4$, $0 \leq x \leq 0.8$) in a number of van Gogh paintings.[16,17] Studies of photochemically aged paint models composed of different chrome yellow varieties revealed that the reduction of Cr(VI) is favored when the pigment is present in the S-rich orthorhombic $PbCr_{1-x}S_xO_4$ (with $x > 0.4$) form.[18,19]

In all the above mentioned studies, μ-XRF maps and single-point μ-XANES spectra in XRF mode were collected by means of traditional energy dispersive (ED) X-ray detectors (*e.g.*, silicon drift detectors (SDDs)/germanium solid-state detectors). These systems reach spectral energy resolutions down to about 140 eV FWHM at the Mn K_α-line (5.9 keV) but are characterized by a limited count rate capability that usually can be up to 5×10^5 counts per s but that may increase to 3–4 $\times$ 10^6 counts per s for other recently developed devices.[20,21] Therefore, during mapping (of XRF signals collected while raster scanning the sample) and XANES (involving scanning of the energy of the primary beam across the absorption edge of the element of interest) experiments, fairly long dwell times per point/pixel or point/energy (*i.e.*, 0.1–1 s) must be respected.[22–24] This can result in extended scanning times (typically of the order of several hours per map and a few minutes per XANES spectrum) and relatively high X-ray doses impinging on the materials. The latter may increase the probability of beam-induced damage in the examined specimen.[25] These non-optimal characteristics of traditional ED-XRF detectors frequently confine the data acquisition in μ-XRF mapping experiments to few and relatively small regions of interest within the sample, with the consequence that the obtained results might not be representative of the entire material. These limitations become even more stringent when XANES mapping experiments are undertaken. A typical experiment of this kind consists of analyzing one or more areas of interest by recording μ-XRF maps at a few (~2–5) different energy values around an absorption edge. Discriminating energies can be selected on the basis of the XANES spectral features of the compounds to be investigated; through manipulation of the resulting XRF maps, a set of chemical state distributions can be obtained. Mapping measurements of this kind are usually combined with collection of single-point XANES spectra in XRF mode at a limited number of locations, thought to be representative of the entire map. *Via* such a procedure, however, the full spectral (FS) XANES response of all examined points in the mapped area is not recorded. Thus, it is possible that the presence of specific species of the element of interest in a subarea of the map may be completely overlooked.

By employing "fast" XRF detectors it is possible to overcome some of the above-mentioned limitations of traditional ED-XRF data acquisition systems. In this category, the Maia-384 massively parallel detector (jointly developed by the Commonwealth Scientific and Industrial Research Organization (CSIRO, Australia) and the Brookhaven National Laboratory (BNL, USA)) occupies a central position.[26–28] The system consists of an annular array of 384 silicon diode detectors positioned in a backscatter geometry with respect to the incident X-ray beam; this geometry ensures that a large (~1.3 sr) solid angle is subtended. An approach based on an event-mode data collection with real-time processing capabilities allows the recording of maps with a minimum dwell time down to ~0.05 ms per pixel and a total count-rate capacity greater than 10 M s^{-1} while avoiding readout overheads. A real-time FS elemental deconvolution can be obtained through an integrated algorithm based on a matrix transform method called dynamic analysis (DA).[29]

The Maia detector has found wide application for performing two-dimensional micrometer-scale resolution elemental mapping experiments over large areas of materials of interest in different scientific fields, such as earth and environment science,[30–33] biology,[34,35] medicine,[36,37] and cultural heritage.[38] It has also allowed micro-tomography[39–41] and XRF-mode XANES imaging[42–45] to be successfully conducted on biological and environmental samples in practical time frames. During XRF mode XANES imaging of this type, chemical speciation information is obtained *via* fast, sequential acquisition of a series of XRF images at the micrometer scale while small incremental changes in energy (E) are made across the absorption edge of the element of interest. After DA elemental deconvolution, the XANES spectra can be extracted at each pixel from the E-stack of images and chemical state maps can be calculated by employing a linear combination fitting procedure against a set of reference spectra. This type of FS-XANES imaging appears in principle optimal for the study of complex and heterogeneous samples such as degraded paint micro-samples. However, so far, this state-of-the-art detector technology has never been employed in the context of artists' pigments alteration studies.

In this paper, Cr K-edge FS-XANES imaging in XRF mode is proposed as a new strategy for studying the nature and

distribution of alteration products of lead chromate-based yellow pigments in painting materials. The aims of the paper are threefold: (i) outline the technical advantages and drawbacks in using either FS-XANES imaging or μ-XRF mapping/single-point μ-XANES investigations in the specific context of the study of altered chrome yellow paints; (ii) evaluate whether or not FS-XANES imaging can contribute to a more representative and reliable identification of the Cr-based alteration compounds and their spatial distribution (through the collection of XANES spectral profiles from all locations in the examined area); (iii) assess if FS-XANES imaging may be used as a reliable method for quantitatively determining the abundance of different Cr species and compare its performance to that of more conventional single-point μ-XANES analysis.

For these purposes, in the following sections, we present and discuss a comparison between FS-XANES imaging data obtained at the Cr K-edge using the Maia X-ray detector and corresponding μ-XRF mapping/single-point μ-XANES results acquired by means of a more conventional SDD. Data were collected during the study of two altered chrome yellow paint micro-samples taken from two paintings by Vincent van Gogh: *Falling Leaves* (*Les Alyscamps*) (Kröller-Müller Museum, Otterlo, The Netherlands) and *The Bedroom* (Van Gogh Museum, Amsterdam, The Netherlands). In addition, similar data recorded from a relevant photochemically aged chrome yellow paint model are also described.

2. Experimental

2.1. Resin-embedded original paint micro-samples and photochemically aged model paint

Investigations were performed on two resin-embedded paint micro-samples taken earlier from darkened chromium-based yellow areas of the following paintings by Van Gogh: *Falling Leaves* (*Les Alyscamps*) (sample 224/1) and *The Bedroom* (sample F482/8) (Fig. 1A and 2A). The sampling locations of these paints are reported in Fig. S1 of the ESI.†

Previous SEM-EDX, micro-FTIR, micro-Raman and SR micro-X-ray diffraction analyses of the selected samples allowed one to demonstrate that chrome yellow is present as a $PbCr_{1-x}S_xO_4$ ($x \sim 0.5$) co-precipitate in sample 224/1, while in F482/8 it occurs as $PbCrO_4$.[46,47]

Measurements were also carried out on a paint model that was prepared by mixing $PbCr_{0.2}S_{0.8}O_4$ with linseed oil in a 4 : 1 weight ratio and by applying the mixture on a polycarbonate microscope slide. In line with previous papers,[17,19,47] this sample is designated henceforth as S_{3D}. The paint model was irradiated using a commercial light source emitting radiation above 400 nm for 21 days. The measured illuminance at the sample position was about 3×10^5 lux. The aged material was prepared and analyzed as a thin section of about 10 μm in thickness (see below, Fig. 8A–C).

2.2. SR-based X-ray investigations at the Cr K-edge

Synchrotron X-ray experiments at the Cr K-edge were performed in two modes: (i) conventional μ-XRF mapping at different energies combined with the acquisition of a few single-point μ-XANES spectra and (ii) FS-XANES imaging in XRF mode. Investigations (i) were carried out at the X-ray microscope beamline ID21 of the European Synchrotron Radiation Facility (ESRF, Grenoble, France)[48] by means of a SDD, while measurements (ii) were carried out at the X-ray fluorescence microscopy (XFM) beamline of the Australian Synchrotron (AS, Melbourne, Australia)[49] and at the hard X-ray micro/nano-probe beamline P06 of the Deutsches Elektronen-Synchrotron (DESY, Hamburg, Germany)[26] using the Maia-384A and Maia-384B detectors, respectively. An overview of the experimental set-up and the conditions used at these three SR end stations are reported in Tables 1 and 2. Further details are provided in the following sections.

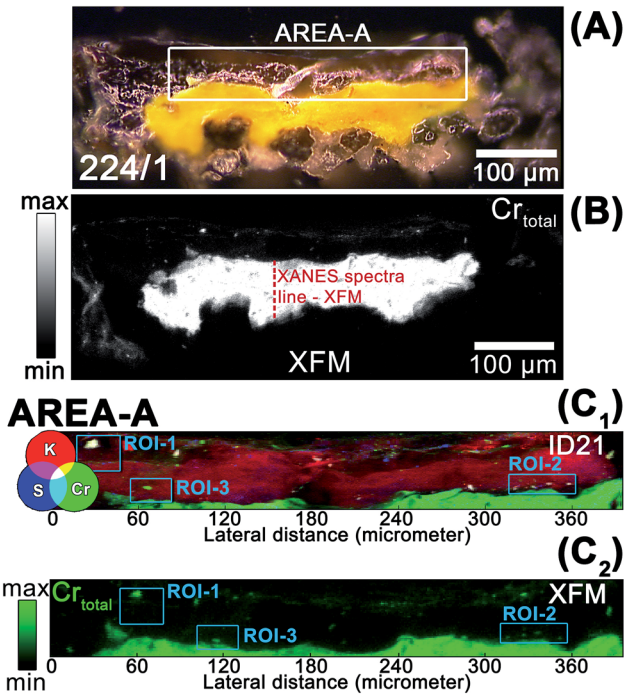

Fig. 1 Sample 224/1 – *Falling Leaves* (*Les Alyscamps*). (A) Photomicrograph and (B) μ-XRF Cr_{total} distribution (6.09 keV) of the entire sample collected following completion of the XRF-mode XANES imaging at the XFM beamline (Maia-384A detector). RGB μ-XRF distribution of (C_1) K/Cr_{total}/S and (C_2) Cr_{total} acquired at the ID21 (silicon drift detector (SDD)) and XFM beamlines, respectively (see Table 2 for experimental details). Maps of (C_1 and C_2) were acquired in the area shown by the white rectangle in (A). In (C_1 and C_2), cyan rectangles indicate the regions were XANES spectra were recorded (see Fig. 3D and E). In (B), the red dotted line illustrates the position where a line of Cr K-edge XANES spectra was extracted from the E-stack of images (see Fig. 4B).

2.2.1. XFM beamline (AS). Original paint micro-samples were analyzed in the 5.96–6.09 keV energy range using a monochromatic primary beam (about $\Delta E/E = 10^{-4}$) produced by means of a Si(111) fixed-exit double-crystal monochromator. Kirkpatrick–Baez (KB) mirrors were used to focus the beam to a spot size of about 2×2 μm^2 ($h \times v$). The beam drift over a 24 hour period is within 3 μm in the horizontal and vertical directions, respectively, and the beam is stable within 1 μm

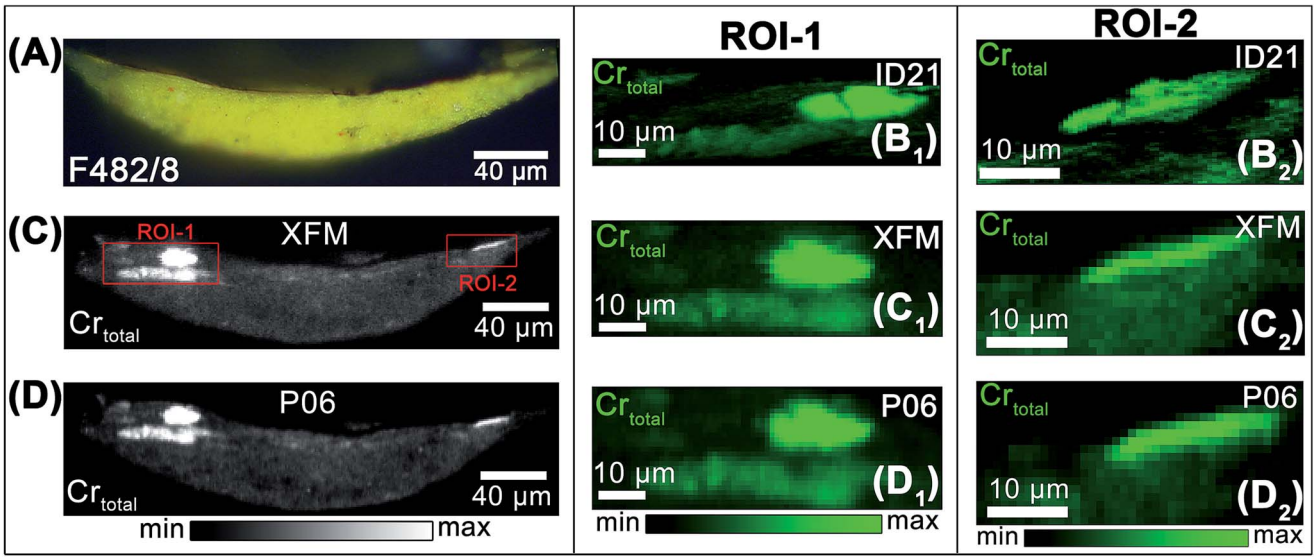

Fig. 2 Sample F482/8 – *The Bedroom*. (A) Photomicrograph and μ-XRF Cr_{total} distribution (6.09 keV) obtained at the beamlines (B_1 and B_2) ID21 (SDD), (C) XFM (Maia-384A detector) and (D) P06 (Maia-384B detector). (C_1–D_2) Magnified maps of ROI-1 and ROI-2 obtained from (C) and (D) (see Table 2 for experimental details).

vertically and 1 μm horizontally in the 5.96–6.09 keV energy range.

The Maia-384A detector had a 375 eV spectral energy resolution at the Mn K_α-line (5.9 keV); scanning was performed with dwell time between 0.5 and 2 ms per pixel. The XRF signal was collected in a backscatter geometry with respect to the incident beam with a solid angle of ~1.3 sr.[28]

A stack of 126 μ-XRF maps was recorded at around the Cr K-edge using the following energy increments: (i) 2 eV below and above the absorption edge (5.9600–5.9810 keV and 6.0200–6.0900 keV) and (ii) 0.5 eV in the region around the pre-edge peak and the absorption edge (5.9810–6.0200 keV).

The deconvolution into elemental maps of the FS-XRF data (XANES stack) was performed using the DA method implemented in GeoPIXE,[50,51] which allowed separation of the respective contributions of the scatter peaks, the Cr K- and Ba L-lines. This software was also employed to correct for the alignment and drifting of frames in the XANES stack. The TXM-Wizard software[52] was used to fit the Cr K-edge XANES spectra for regions of interest in the XANES stacks exported from GeoPIXE (each profile obtained by averaging not more than 60 single pixel XANES spectra) and to produce chemical state maps. XANES spectra of Cr(VI) compounds present an intense pre-edge peak at 5.993 keV and the absorption edge position shifted about 5 eV towards higher energies compared to Cr (III) compounds.[18] Therefore, after determination of edge-jump, noise filtering and normalization, Cr phase maps were obtained by describing the XANES spectra at each pixel as a least squares linear combination (LSLC) of a set of XANES spectra of Cr(VI) and Cr(III) reference compounds. The

Table 1 Experimental set-up conditions used for performing Cr-speciation investigations (5.96–6.09 keV energy spectral range) at the beamlines XFM (AS, Melbourne, Australia), P06 (DESY, Hamburg, Germany) and ID21 (ESRF, Grenoble, France)

Beamline (SR facility)	Focusing optics	Beam size ($h \times v$) (μm^2)	Change of beam position during a scan ($h \times v$) (μm^2)	Detector	Active area/ solid angle	Geometry	Energy resolution at 6 keV (eV)	Dwell time (ms per pixel)	Attenuated photon flux[g] (ph s^{-1})
XFM (AS)	KB mirrors	2 × 2	~3 × 3[b]	Maia 384A	384 mm^2/ ~1.3 sr	180°-backscattering	375	0.5–2	~1–3 × 10^8
P06 (DESY)[a]	KB mirrors	0.7 × 0.6	~4 × 3[c]	Maia 384B	384 mm^2/ ~1.3 sr	180°-backscattering	290	0.5–3[e]	~4 × 10^6; ~9 × 10^8
ID21 (ESRF)[a]	Fresnel zone plates	Down to 0.6 × 0.2	~0.3 × 0.5[d]	Silicon drift diode (Xflash 5100, Bruker)	80 mm^2/ few 10^{-2} sr	Incident angle: 62°, detection angle: 69°	150–170	100–300[f]	~2–9 × 10^8

[a] Measurements carried out during 2 different experiments (see Table 2 for additional details). [b] Value measured over a 24 hour period. [c] Value measured over a 9 hour period. [d] The change of the beam position was measured as a function of energy. [e] Typical range values are: 0.5–50 ms per pixel. [f] Typical range values are: 0.1–2 s per pixel. [g] Values obtained using attenuators/slits. Maximum flux of about 10^{10} to 10^{11} ph s^{-1}.

Table 2 Comparison among the experimental conditions employed for the acquisition of the XRF maps of original paint micro-samples at the beamlines XFM (AS), P06 (DESY) and ID21 (ESRF)

Sample	Maps	Map size ($h \times v$) (μm^2)	Pixel size ($h \times v$) (μm^2)	Pixel total number	Dwell time (ms per pixel)	Acquisition time per energy scan (min:s)	Acquisition time[a] (min)	Absolute photon flux (ph s^{-1})	Dose per energy scan (ph μm^{-2})	Dose[a] (ph μm^{-2})
224/1 *Falling Leaves* (*Les Alyscamps*)	Entire sample$_{XFM}$ (Fig. 1B)	610 × 230	1 × 1	1.403×10^5	0.49	2:23	300	1.3×10^8	$\sim 6.3 \times 10^4$	$\sim 8 \times 10^6$
	AREA-A$_{XFM}$ (Fig. 1C$_1$)	395 × 53	1 × 1	2.0935×10^4	1.96	1:12	150	2.7×10^8	$\sim 5.3 \times 10^5$	$\sim 6.7 \times 10^7$
	AREA-A$_{ID21}$ (Fig. 1C$_2$)	395 × 54	1 × 0.5[c]	4.266×10^4	150	110:00	215	9.2×10^8	$\sim 2.3 \times 10^8$	$\sim 4.6 \times 10^8$
F482/8 *The Bedroom*	Entire sample$_{XFM}$ (Fig. 2C)	300 × 80	1 × 1	2.4×10^4	0.99	1:00	130	2.1×10^8	$\sim 2 \times 10^5$	$\sim 2.6 \times 10^7$
	Entire sample$_{P06}$ (Fig. 2D)	300 × 80	1 × 1	2.4×10^4	3	1:40	210	9×10^8	$\sim 6.4 \times 10^6$	$\sim 8 \times 10^8$
	ROI-1$_{XFM}$[b] (Fig. 2C$_1$)	73 × 24	1 × 1	1.752×10^3	0.99	0:04	10	2.1×10^8	$\sim 2 \times 10^5$	$\sim 2.6 \times 10^7$
	ROI-1$_{P06}$[b] (Fig. 2D$_1$)	73 × 24	1 × 1	1.752×10^3	3	0:07	15	9×10^8	$\sim 6.4 \times 10^6$	$\sim 8 \times 10^8$
	ROI-1$_{ID21}$ (Fig. 2B$_1$)	73.8 × 22.6	0.6 × 0.2[d]	1.3899×10^4	150[e]	36:00	108	1.7×10^8	$\sim 1.5 \times 10^7$	$\sim 3.3 \times 10^7$
					300[f]	72:00			$\sim 1.8 \times 10^7$	
	ROI-2$_{XFM}$[b] (Fig. 2C$_2$)	41 × 18	1 × 1	7.38×10^2	0.99	0:02	4	2.1×10^8	$\sim 2 \times 10^5$	$\sim 2.6 \times 10^7$
	ROI-2$_{P06}$[b] (Fig. 2D$_2$)	41 × 18	1 × 1	7.38×10^2	3	0:03	6–7	9×10^8	$\sim 6.4 \times 10^6$	$\sim 8 \times 10^8$
	ROI-2$_{ID21}$ (Fig. 2B$_2$)	40.8 × 18	0.6 × 0.2[d]	6.12×10^3	150[e]	17:00	50	1.7×10^8	$\sim 3 \times 10^7$	$\sim 8 \times 10^7$
					300[f]	33:00			$\sim 5 \times 10^7$	

[a] Values refer to the acquisition of 126 XRF images for the measurements performed at XFM and P06 beamlines, and to that of 2 images for the analysis carried out at ID21. [b] Magnified area selected from the larger map collected from the entire sample. [c] Beam sizes ($h \times v$) of 0.74×0.23 μm^2. [d] Beam sizes ($h \times v$) of 0.6×0.2 μm^2. [e] At 6.09 keV. [f] At 5.993 keV.

combination yielding the best fit quality (checked on the basis of the chi-square, reduced chi-square and *R*-factor values) was chosen as the most likely set of Cr compounds present at that location.

2.2.2. P06 beamline (DESY). Paint micro-sample F482/8 (from *The Bedroom*) and the aged paint model were investigated by employing a version of the Maia detector (384B) having a better spectral energy resolution (290 eV at Mn-K$_\alpha$) that was recently installed at the PETRA-III P06 end station. This system already was successfully used for studying complex natural samples.[26,53] It also enables the detection of X-rays at lower energies (down to 2.0 keV rather than 3.3 keV) compared with the Maia-384A model (XFM beamline) (see Section 2.2.1 and Table 1).

During the P06 investigations, a monochromatic primary beam (about $\Delta E/E = 10^{-4}$) in the 5.9–6.0 keV energy range was obtained by means of a Si(111) fixed-exit double-crystal monochromator. KB mirrors were used to focus the beam to a spot size of about 0.7×0.6 μm^2 ($h \times v$). The position of the sample relative to the beam drifted over a 9 hour period by 4 μm in the horizontal direction and 3 μm in the vertical plane.

By employing dwell times between 1 and 3 ms per pixel, FS-XANES imaging experiments and corresponding data elaboration were performed using the same experimental conditions and software packages as those described above for the XFM investigations (see Section 2.2.1).

2.2.3. ID21 beamline (ESRF). In order to produce a highly monochromatic primary beam (with $\Delta E/E = 10^{-4}$), a Si(220) fixed-exit double-crystal monochromator was employed. The incident beam was focused with Fresnel zone plates down to a size of 0.6×0.2 μm^2 ($h \times v$) and maintained stable within 0.5 μm vertically and 0.3 μm horizontally across the Cr K-edge (5.96–6.09 keV).

XRF signals were collected in the horizontal plane and at 69° with respect to the incident beam direction by using a single energy-dispersive SDD (Xflash 5100, Bruker with Moxtek thin polymer window). This data acquisition device is characterized by an active area of 80 mm^2, a spectral energy resolution ranging from 150 to 170 eV at 5.9 keV (depending on the electronics configuration), a maximum count rate up to 10^5 per second and sample-solid angle values of the order of a few 10^{-2} sr.[24] Two-dimensional μ-XRF maps were obtained *via* raster scanning of the samples using the focused X-ray beam and with dwell times in the 100–300 ms range. Elemental distributions were produced employing the PyMca software,[54] among others, to resolve the overlap between the Cr–K and Ba-L lines and the scatter peaks.

To obtain chemical state distributions, the energy of the incoming X-rays was set to two fixed energy values close to the Cr K-edge, where the absorption and consecutively the XRF of particular Cr species are optimal: (i) at 5.993 keV, for favoring the excitation of only the Cr(VI) species, and (ii) at 6.090 keV in order to obtain XRF signals originating from all chromium species. The procedure that was used to produce the Cr chemical state maps is described elsewhere.[18]

Single-point μ-XANES spectra were acquired in XRF mode by scanning the primary energy in the 5.96–6.09 keV range

and using energy increments of 0.2 eV. For all profiles, the procedure of normalization was performed by means of ATHENA.[55] The same software was also used to carry out a linear combination fitting of the spectra against a library of XANES profiles of Cr reference compounds. Preliminary tests were performed in order to avoid beam-induced damage of samples.

Regarding sample 224/1 (from *Falling Leaves* (*Les Alyscamps*)) (see Section 3.2.1), a detailed discussion of the Cr-speciation results obtained at the ID21 beamline is reported elsewhere.[17] Thus, in what follows, only a selection of these data will be presented and compared with the corresponding ones collected at the XFM beamline.

3. Results and discussion

3.1. Two-dimensional μ-XRF chromium distributions of original paint micro-samples

Table 2 summarizes the experimental conditions used for performing SR μ-XRF mapping around the Cr K-edge of samples 224/1 (from *Falling Leaves* (*Les Alyscamps*)) (Fig. 1A) and F482/8 (from *The Bedroom*) (Fig. 2A) at the XFM (Maia-384A), P06 (Maia-384B) and ID21 (SDD) beamlines. The corresponding Cr distributions recorded at 6.09 keV (*i.e.*, above the Cr absorption edge; a single energy scan is provided as an example) are presented in Fig. 1B–C_2 and 2B_1–D_2. In the following sections, these data sets will be used to describe and compare the technical features of the different experimental set-ups in terms of acquisition times, radiation doses, spatial resolution and effects related to their detection geometry.

3.1.1. Acquisition time. As illustrated in Table 2, by using the Maia-384A detector (XFM), the 126 incident E-stack of images around the Cr K-edge (5.96–6.09 keV) of the entire sample 224/1 (610 × 230 μm^2) took about 300 minutes to record (approximately 2 min for each energy scan). Using both versions of the Maia detector, a similar experiment was conducted to scan the entire area (300 × 80 μm^2) of sample F482/8; this took around 130 and 210 minutes for the XFM and the P06 detectors, respectively (*i.e.*, less than 2 min for each energy scan; see Table 2 for further details). For 224/1 and F482/8, the corresponding Cr total distribution recorded at 6.09 keV is shown in Fig. 1B and 2C and D. The possibility to map the entire sample within a practical time frame (*i.e.*, taking not more than 5 hours for the acquisition of the entire E-stack of images) allowed a complete overview of the Cr distribution to be obtained (see Section 3.2 for details).

Fig. 1C_1 and C_2 and 2B_1–D_2 show a comparison between the total Cr distribution acquired from equivalent regions of interest of samples 224/1 and F482/8 using the SDD/ID21, Maia-384A/XFM and Maia-384B/P06 set-ups. According to the values shown in Table 2, for equal dimensions of the scanned areas but different pixel sizes (down to 0.6 × 0.2 μm^2 for the data sets obtained at ID21), acquisition times of the Maia detector (XFM, P06) are a factor of 10^2 to 10^3 shorter than those of the SDD (ID21). The result is that during the Maia detector-based experiments, the collection of a stack of 126 maps could be completed in a scanning time that is up to about 10 times shorter than that required to record equivalent maps at only two different energies (*i.e.*, at 5.993 and 6.09 keV) by means of the SDD-based system.

3.1.2. Radiation dose. As a result of the reduced dwell time (0.5–3 ms per pixel) of the Maia detector (XFM, P06), the delivered X-ray dose (expressed as ph μm^{-2}) per energy scan to the sample is also a factor of 10^4 to 10^2 lower than those of SDD-based investigations at ID21. As Table 2 summarizes, for the experiment conducted at XFM (flux ∼ 1–3 × 10^8 ph s^{-1}), the X-ray dose ranges from 6.3 × 10^4 ph μm^{-2} (0.5 ms dwell time) to about 2–5 × 10^5 ph μm^{-2} (1.96 ms dwell time), while it is at around 6 × 10^6 ph μm^{-2} (3 ms dwell time) for experiments carried out at P06 (flux ∼ 9 × 10^8 ph s^{-1}). Regarding the ID21 investigations, depending on both the beam size and dwell times (see Table 2 for further details) the dose per energy scan ranges from 1.5 × 10^7 to 2.3 × 10^8 ph μm^{-2} (flux ∼ 2–9 × 10^8 ph s^{-1}). It follows that for the acquisition of an E-stack of 126 maps by means of the Maia detector-based set-ups an X-ray dose of about the same order of magnitude or slightly higher (*i.e.*, not more than a factor of 10) was required with respect to the collection of a set of images at 2 different energies using the SDD-based system (Table 2). It is worth mentioning that the flux on the samples was reduced with a set of slits or attenuators during the investigations at the three SR end-stations (flux without using attenuators/slits down to about 10^{10} to 10^{11} ph s^{-1}). Moreover, after investigations, none of the analyzed samples showed any evidence of beam-induced damage under the experimental conditions employed at the three SR facilities.

3.1.3. Spatial resolution and experimental set-up geometry effects. As shown in Fig. 1 and 2, the spatial resolution achieved for the data sets collected using the Maia-384A/XFM (beam size of approximately 2 × 2 μm^2) and Maia-384B/P06 (beam size of about 0.6 × 0.7 μm^2) set-ups do not allow clear revealing of some features of 5–10 μm dimensions that are on the contrary clearly visible in the corresponding higher-resolution maps acquired by means of the SDD/ID21 microprobe system (beam size down to 0.6 × 0.2 μm^2). Obviously the lateral resolution is in the first place determined by the dimensions of the primary beam and only in the second place by the noise level in the resulting elemental/species-specific maps. Regardless of the type of experimental set-ups employed, the recorded Cr distributions are similar within the yellow paint, while the shape and size of the Cr-rich grains localized inside the superficial varnish layer (sample 224/1, Fig. 1C_1 and C_2, ROI-1, ROI-2, ROI-3; see Fig. 5 of ref. 17 for the corresponding maps collected at ID21) or nearby the surface (sample F482/8, Fig. 2B_1–D_2) are not optimally visualized in the Maia-384A/XFM maps. As Fig. 2D_1 and D_2 illustrate, because of the longer dwell time and higher flux used at P06, as well as the increased sensitivity provided by the higher spectral energy resolution of the Maia-384B detector, P06 data do show maps with a slightly improved clarity relative to those obtained at the XFM beamline (Fig. 2C_1 and C_2); on the other hand, Maia-384B/P06 distributions show a definition lower than would be expected (see Fig. 2B_1 and B_2 for a comparison with the equivalent higher resolution ID21 images) due to the

fact that maps were recorded using a step size (1×1 μm^2) larger than that of the beam (0.6×0.7 μm^2).

Moreover, changes in the relative positions of Cr grains can be observed, such as those for example present in Fig. 1C$_1$ and C$_2$ (*cf.* ROI-1, ROI-2 and ROI-3) and Fig. 2B$_1$–D$_2$. The apparent displacement is ascribable to the different geometry of the Maia- and SDD-based experimental set-ups (*cf.* Table 1) and occurs both in the horizontal and vertical direction as a function of the depth of the particles below the paint surface.

Summarizing, as a result of the shorter dwell times per pixel (0.5–3 ms), the Maia detector-based microprobe systems allow for scanning of large sample areas with acquisition times and X-ray doses that are up to 2–3 orders of magnitude lower than those of the SDD-based system. On the other hand, the more limited lateral resolution of the Maia-384A/XFM and Maia-384B/P06 set-ups does not allow resolution of fine details below the level of some micrometers while such details are clearly visible in the maps collected using the SDD/ID21 system.

On the basis of the technical features mentioned above, in the next section, the Cr speciation in original paint micro-samples and a photochemically aged chrome yellow paint model sample will be discussed through the comparison between the Cr K-edge FS-XANES imaging results acquired using the Maia-384A/XFM and Maia-384B/P06 set-ups and μ-XRF mapping/single-point μ-XANES data obtained by means of the SDD/ID21 microprobe system.

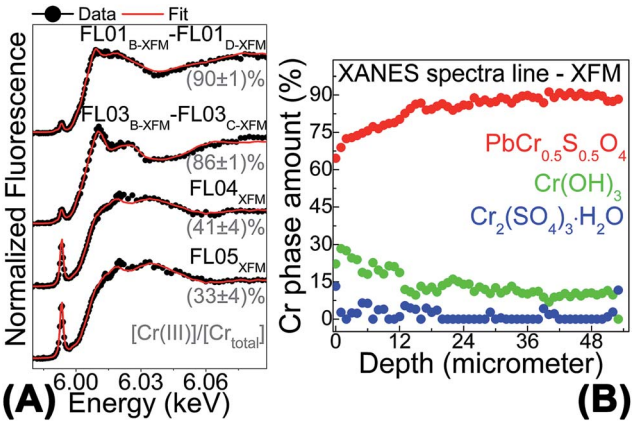

Fig. 4 Additional Cr K-edge FS-XANES data extracted from 224/1. (A) Profiles (black) (number of averaged pixels: 20–30; pixel sizes: 1×1 μm^2; dose: ~7×10^7 ph μm^{-2}) and corresponding result of the linear combination fitting (red) of $PbCr_{0.5}S_{0.5}O_4$, $Cr(OH)_3$ and $Cr_2(SO_4)_3 \cdot H_2O$ as reference compounds (see Fig. 3A and Table S1†). (B) Percentage relative amount of different Cr phases *vs.* the depth obtained by linear combination fitting of the single-pixel XANES spectra extracted from the region of the images stack shown in Fig. 1B.

3.2. Cr speciation in original paint micro-samples and in an aged paint model

Fig. 3–7 show the Cr chemical state maps and XANES spectra obtained from original paint micro-samples 224/1 and F482/8. These data were acquired from the areas shown in Fig. 1 and 2.

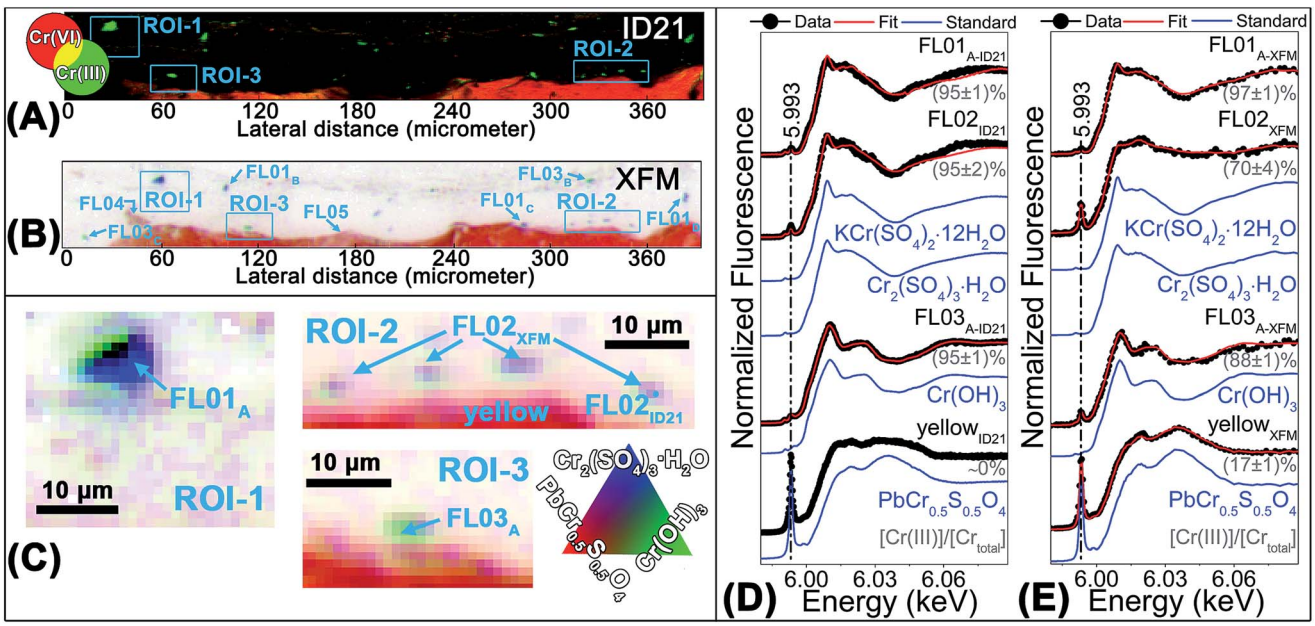

Fig. 3 Cr-speciation results of 224/1. (A) Cr(VI)/Cr(III) chemical state maps acquired at ID21 (see Fig. 1C$_1$). (B) Quantitative Cr phase maps and (C) corresponding magnification of the regions of interest (see also ref. 17 for further details) obtained from the linear combination fitting of the XANES stack collected at the beamline XFM using the profiles of $PbCr_{0.5}S_{0.5}O_4$ (red), $Cr(OH)_3$ (green) and $Cr_2(SO_4)_3 \cdot H_2O$ (blue) as reference compounds (see Fig. 1C$_2$). RG result of the fit (red) of the XANES profiles by linear combination of $PbCr_{0.5}S_{0.5}O_4$, $Cr(OH)_3$ and $Cr_2(SO_4)_3 \cdot H_2O$ (blue) to the spectra (black) obtained at (D) ID21 (beam size ($v \times h$): 0.23×0.74 μm^2; dose: ~3.5×10^{12} ph μm^{-2}) and (*E*) XFM (number of averaged pixels: 3–30; pixel sizes: 1×1 μm^2; dose: ~7×10^7 ph μm^{-2}). Measurement positions are shown in (B and C) by cyan arrows and labels. In (D and E), grey labels show the percentage relative amount of Cr(III) (see Table S1 of the ESI† for details).

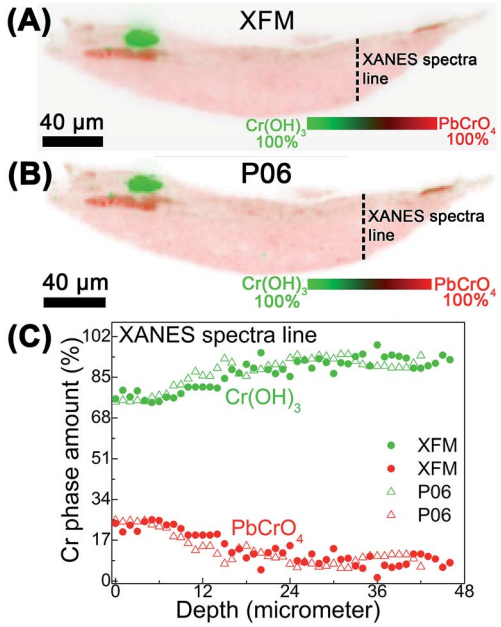

Fig. 5 Cr-speciation results of F482/8. Quantitative Cr phase maps obtained from the linear combination fit of the Cr K-edge XANES stack collected at (A) XFM and (B) P06 using the profiles of $PbCrO_4$ (red) and $Cr(OH)_3$ (green) as reference compounds (see Fig. 2C and D). (C) Percentage relative amount of $PbCrO_4$ (red) and $Cr(OH)_3$ (green) *vs.* the depth obtained by linear combination fitting of the single-pixel XANES spectra extrapolated from the region shown in (A) (circles) and (B) (triangles).

The results arising from similar investigations of the aged paint model are reported in Fig. 8.

The relative abundance of Cr species (expressed as [Cr(III)]/[Cr_{total}]) was obtained by LSLC fitting of the XANES spectra and data are summarized in Tables S1 and S2 of the ESI.†

3.2.1. Sample 224/1 (*Falling Leaves* (*Les Alyscamps*)). Fig. 3B shows the quantitative Cr phase maps obtained from the FS-XANES imaging experiment carried out at XFM. These images were obtained by LSLC fitting of each individual XANES spectrum extracted from the E-stack of images against the XANES profiles of $PbCr_{0.5}S_{0.5}O_4$ (red in Fig. 3B and C), $Cr(OH)_3$ (green) and $Cr_2(SO_4)_3 \cdot H_2O$ (blue) as reference compounds. In line with earlier investigations[17] and the XANES spectra of Fig. 3D and E (see below), using these components in the fit model yielded the best results. The phase maps illustrate that the lead chromate-based compound is mainly localized in the yellow paint, while Cr(III)-rich particles, present as $Cr_2(SO_4)_3 \cdot H_2O$ and $Cr(OH)_3$ compounds, are localized both close to the paint/varnish interface and inside the varnish (see also magnified areas of ROI-1, ROI-2 and ROI-3 in Fig. 3C).

The corresponding Cr(III) and Cr(VI) chemical state maps obtained at ID21 (Fig. 3A) show a similar distribution as those of Fig. 3B, but at a higher spatial resolution. Inside the varnish, reduced Cr is often associated with the presence of K and S (Fig. $1C_1$; ROI-1 and ROI-2).

In Fig. 3D and E (black data points) a selection of the μ-XANES spectra recorded at ID21 (see ref. 17 for additional data) are compared to the equivalent ones extrapolated from the XANES stack collected at XFM (*cf.* Fig. 3B and C to see the corresponding Cr phase maps). For each profile, the result of the corresponding LSLC fitting (red lines) is also shown (see Table S1 of the ESI† for further details).

The XANES spectra obtained from a Cr(III) particle inside the varnish (Fig. 3C–E, ROI-1, $FL01_{A\text{-}ID21/XFM}$) yielded comparable quantitative fitting results, revealing that Cr is present as about 95–97% of Cr(III) (Table S1†); the spectral features mainly resemble those of a Cr(III) sulfate-based compound, such as $KCr(SO_4)_2 \cdot 12H_2O$ or $Cr_2(SO_4)_3 \cdot H_2O$ (Fig. 3D and E, blue lines). The data obtained by averaging the single pixel XANES profiles in correspondence of three additional varnish-embedded micro-grains show similar characteristics, revealing an abundance of $Cr_2(SO_4)_3 \cdot H_2O$ at around 90% (Fig. 3B and 4A, $FL01_{B\text{-}XFM}$–$FL01_{D\text{-}XFM}$ and Table S1;† no corresponding ID21 profiles available).

In another area inside the surface coating (Fig. 3C, ROI-2), a Cr(III) sulfate-based compound was estimated to be present as well. From the ID21-collected spectrum (Fig. 3D, $FL02_{ID21}$), the relative abundance of this compound was estimated to be around 95%, while a value of around 70% is derived from the corresponding data obtained at XFM (Fig. 3E, $FL02_{XFM}$). Close to the yellow paint surface (Fig. 3C, ROI-3), the profiles recorded from another particle resemble that of $Cr(OH)_3$ (Fig. 3D, $FL03_{A\text{-}ID21/XFM}$). In this region, the relative amount of Cr(III) is 95% and 88% for the data obtained at ID21 and XFM, respectively (Table S1†). Two micro-grains of similar composition were found to be present in other areas of the varnish, as demonstrated by the corresponding average spectrum (Fig. 4A, $FL03_{B\text{-}XFM}$–$FL03_{C\text{-}XFM}$ and Table S1;† ID21 profiles not available).

Inside the yellow paint underneath the surface (Fig. 3C, ROI-2, yellow), the spectral features are more similar to that of the $PbCr_{0.5}S_{0.5}O_4$ reference compound (Fig. 3D and E, $yellow_{ID21/XFM}$). While no evidence of the presence of Cr(III) species could be observed in the profile recorded at ID21 (Fig. 3D, $yellow_{ID21}$), their abundance is at around 20% in the corresponding profile obtained at XFM (Fig. 3E, $yellow_{XFM}$ and Table S1†).

In different yellow areas of the paint at the interface with the varnish (Fig. 4A, $FL04_{XFM}$–$FL05_{XFM}$; ID21 profiles not acquired), the FS-XANES data revealed a relatively high abundance (30–40%) of Cr(III) compounds (Cr(III) sulfates and/or $Cr(OH)_3$) (see Table S1†). Analysis of a series of Cr K-edge XANES spectra extracted from the stack of images along a single line perpendicular to the exposed surface of the sample (Fig. 1B) reveals that the total amount of reduced Cr is at around 20–35% within the first 10 μm of the cross-section and progressively decreases with depth, reaching values down to 10% inside the yellow bulk of the paint (Fig. 4B).

On the basis of the good agreement between the abundances of reduced Cr species estimated by means of FS-XANES at XFM and those determined by means of individual μ-XANES spectra at ID21, we can conclude that FS-XANES imaging investigations provide reliable Cr-speciation results. The different spatial resolution and set-up geometry between the Maia-384/XFM and SDD/ID21 datasets (see Tables 1 and 2) justify the variance in the fraction of Cr(III) that is observable in some of the XANES

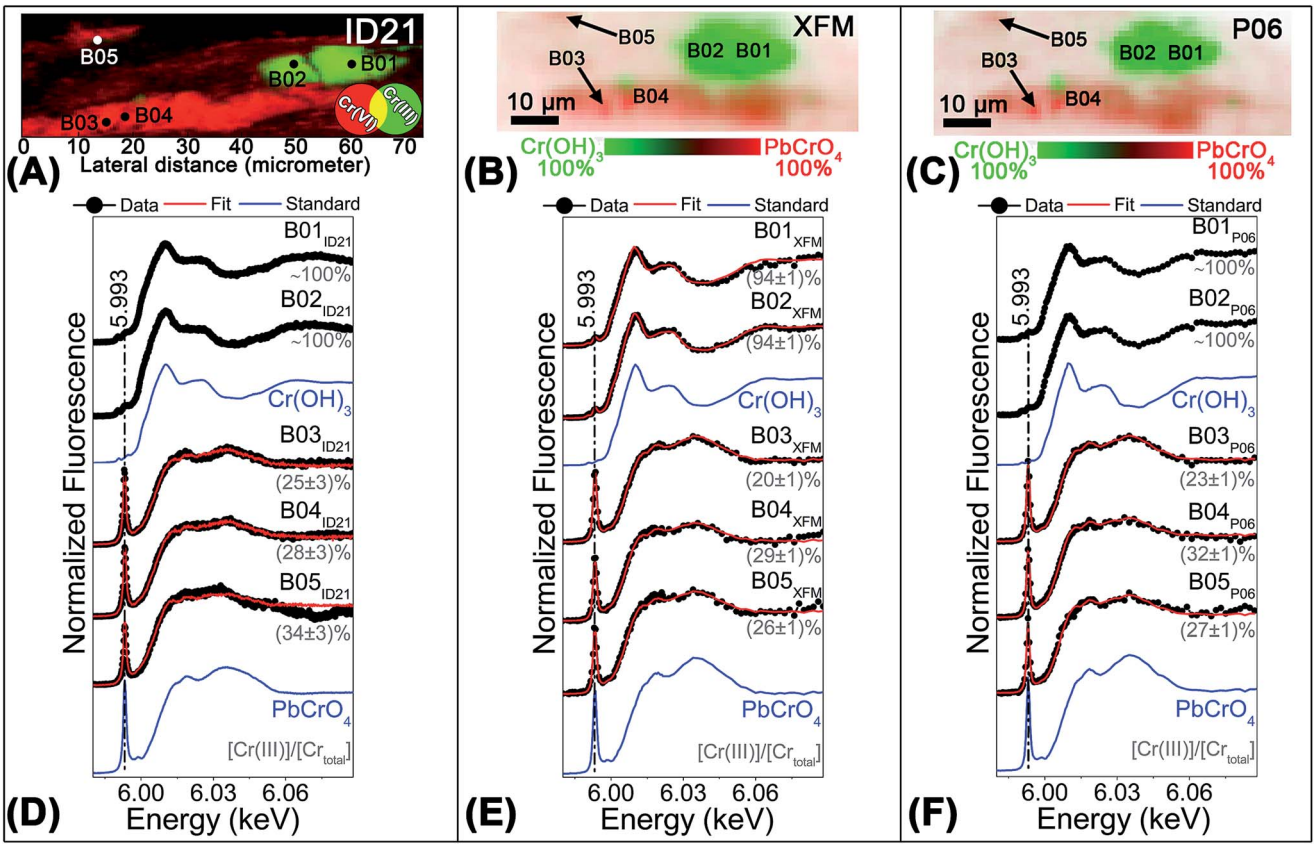

Fig. 6 Cr-speciation results of F482/8: ROI-1. (A) RG Cr(VI)/Cr(III) chemical state maps collected at ID21 and (B) quantitative Cr phase maps obtained from the linear combination fitting of the Cr K-edge XANES stack acquired at (B) XFM and (C) P06 using the profiles of $PbCrO_4$ (red) and $Cr(OH)_3$ (green) as reference compounds (see Fig. $2C_1$ and D_1). Result of the fit (red) of the XANES profiles by linear combination of $PbCrO_4$ and $Cr(OH)_3$ (blue) to the spectra (black) collected at (D) ID21 (beam size ($v \times h$): $0.2 \times 0.6\ \mu m^2$; dose: $\sim 4 \times 10^{11}$ to 2×10^{12} ph μm^{-2}), (E) XFM and (F) P06 (number of averaged pixels: 3–11; pixel sizes: $1 \times 1\ \mu m^2$; $dose_{XFM}$: $\sim 2.6 \times 10^7$ ph μm^{-2}; $dose_{P06}$: $\sim 8 \times 10^8$ ph μm^{-2}). Measurement positions are shown in (A–C) by arrows and labels. In (D–F) grey labels show the percentage relative amount of Cr(III) (see Table S2† for details).

data collected from similar areas using the different microprobe systems (*e.g.*, *cf.* $FL02_{XFM}/FL02_{XFM}$; $yellow_{XFM}/yellow_{ID21}$). It is important to note that the different angles of incidence and collection of the beams at ID21 (62° incident angle; 69° collection angle) and XFM/P06 (normal incidence) mean that different paths are probed into the sample.

By recording spectral data over the entire scanned area, XANES imaging also contributes towards obtaining a more representative overview of the nature and distribution of different Cr compounds. The presence of $Cr(OH)_3$ and Cr(III) sulfates, present either in the form of small particles at the varnish/paint interface or as a layer of about 10 μm in thickness at the yellow paint surface, strongly supports the hypothesis that these are products of the degradation process of the original lead chromate-based pigment.

3.2.2. Sample F482/8 (*The Bedroom*). The quantitative Cr phase maps obtained by LSLC fitting analysis of the XANES stack obtained at the XFM and P06 beamlines are reported in Fig. 5A and B. The XANES profiles of $PbCrO_4$ (red in Fig. 5) and $Cr(OH)_3$ (green) were used as components of the fit. Despite the better spatial and energy resolution of the Maia-384B/P06 microprobe system, a comparable content of information was obtained from the equivalent data set recorded using the Maia-384A/XFM setup, in part likely due to the same step sizes ($1 \times 1\ \mu m^2$) used for collecting the maps. Notably, $PbCrO_4$ is homogeneously present within the yellow paint, while $Cr(OH)_3$ is concentrated in a superficial grain and, to a lesser extent, in other regions close to the paint surface (Fig. 6B and C and 7B and C; see discussion below about the corresponding quantitative fit results). In the two latter areas, the chemical speciation maps obtained from the μ-XRF mapping experiments performed at ID21 (Fig. 6A and 7A) illustrate a similar distribution of Cr(VI) and Cr(III) species at higher spatial resolution.

The single-point μ-XANES spectra acquired at ID21 within these areas are shown in Fig. 6D and 7D. These profiles are compared to the equivalent ones extrapolated by the XANES stack obtained at XFM and P06 (Fig. 6E and F and 7E and F). Although in some locations the apparent grain displacement rendered comparison with the areas analyzed at ID21 less straightforward, the XANES profiles (black data points in Fig. 6 and 7) show similar spectral features. The corresponding fit (red line) yielded comparable results in terms of $[Cr(III)]/[Cr_{total}]$ ratio, with differences that are within ±10% of each other (see Table S2† for further details).

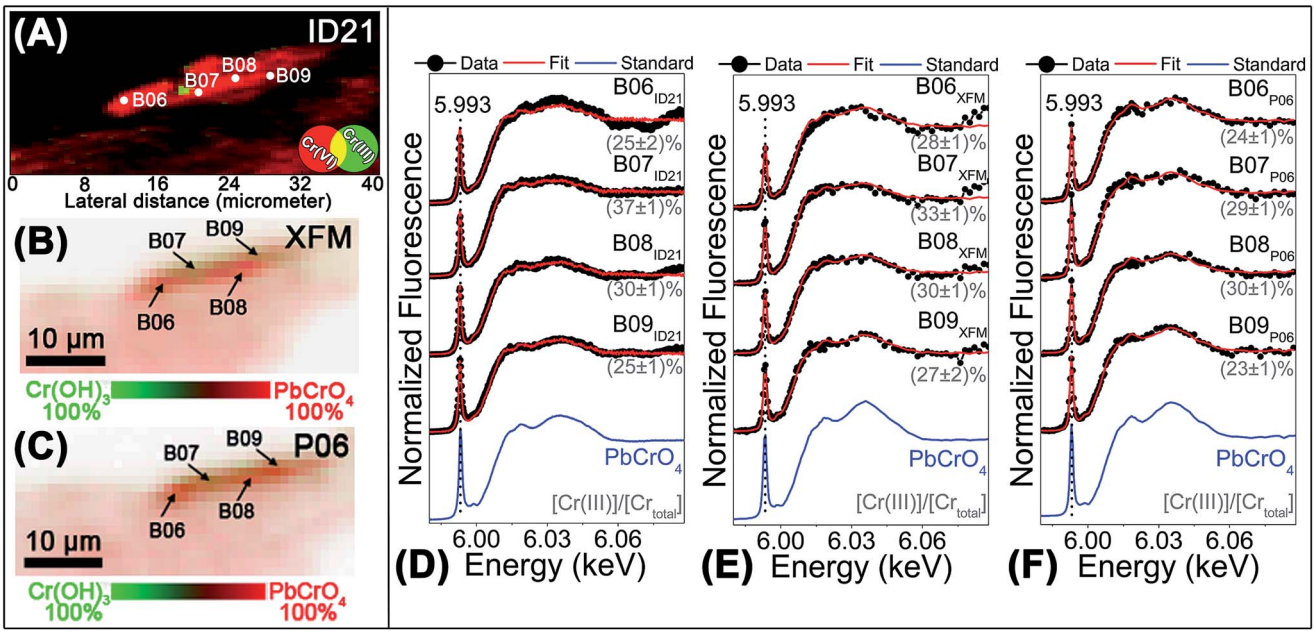

Fig. 7 Cr-speciation results of F482/8: ROI-2. (A) RG Cr(VI)/Cr(III) chemical state maps obtained at ID21 and (B) quantitative Cr phase maps obtained from the linear combination fit of the Cr K-edge XANES stack collected at (B) XFM and (C) P06 using the profiles of $PbCrO_4$ (red) and $Cr(OH)_3$ (green) as reference compounds (see Fig. $2C_2$ and D_2). Result of the fit (red) of the XANES profiles by linear combination of $PbCrO_4$ and $Cr(OH)_3$ (blue) to the spectra (black) collected at (D) ID21 (beam size ($v \times h$): 0.2×0.6 µm^2; dose: $\sim 1.4 \times 10^{12}$ ph µm^{-2}), (E) XFM and (F) P06 (number of averaged pixels: 3–6; pixel sizes: 1×1 µm^2; $dose_{XFM}$: $\sim 2.6 \times 10^7$ ph µm^{-2}; $dose_{P06}$: $\sim 8 \times 10^8$ ph µm^{-2}). Measurement positions are shown in (A–C) by black arrows and labels. In (D–F) grey labels show the percentage relative amount of Cr(III) (see Table S2† for details).

As shown in Fig. 6 (ROI-1), the grain appears to be completely reduced to the Cr(III) state (about 94–100%); the corresponding XANES spectra strongly resemble that of $Cr(OH)_3$ (Fig. 6D–F, B01-02). Profiles collected from other areas adjacent to this particle (B03-05) are more similar to that of $PbCrO_4$ and indicate an amount of $Cr(OH)_3$ of around 20–35% (Table S2†). In another region at the paint surface (Fig. 7, ROI-2), the fit of the XANES spectra (Fig. 7D–F, B06-09) yielded a Cr(III) abundance in the range 25–40% (Table S2†).

The LSLC fitting of a line of single-pixel XANES spectra (Fig. 5C), obtained from a line perpendicular to the exposed surface of the sample (Fig. 5A and B), shows that the relative abundance of $Cr(OH)_3$ is around 25% along the first 7–8 µm of the cross-section; this value progressively decreases with depth, reaching values down to 5% inside the yellow bulk of the sample. In addition, the fit yielded comparable results for both the XFM and P06 data sets.

On the basis of these investigations, the presence of $Cr(OH)_3$ in the form of particles both near the paint surface and as a layer of about 7–8 µm in thickness in the upper part of the yellow paint suggests that this compound is the product of the degradation process of the original lead chromate pigment. Considering that in this and some of the other samples that were examined (see Section 3.2.1 and ref. 17) this compound shows a similar distribution, we do not assume it was originally present (for example in the form of viridian ($Cr_2O_3 \cdot 2H_2O$), a pigment also frequently employed by Van Gogh).[56,57]

In the following section, the results obtained from original paint micro-samples will be complemented by comparing Cr K-edge FS-XANES imaging and single-point µ-XANES data collected from an artificially aged chrome yellow paint model.

3.2.3. Artificially aged chrome yellow paint model. Fig. 8A and B show a photograph of the S_{3D} ($PbCr_{0.2}S_{0.8}O_4$) paint model before and after photochemical aging and a photomicrograph of a thin section obtained from the aged sample. As described elsewhere,[19] after light exposure, this material becomes darker, due to the formation of a brown alteration layer at the exposed surface (Fig. 8B). In view of the limited thickness (about 4–5 µm) of this layer, the Maia-384B/P06 microprobe was used to record a high-definition Cr K-edge FS-XANES image set at ~0.6 µm spatial resolution.

In Fig. 8C and D the area investigated and the resulting quantitative Cr phase maps are shown. Consistent with earlier investigations[19] and with the single-point µ-XANES spectra collected at ID21 along a line from the exposed surface of the paint (Fig. 8E), the best LSLC fitting result was obtained by including the XANES profiles of $PbCr_{0.2}S_{0.8}O_4$ (red in Fig. 8D), $Cr(OH)_3$ (green) and Cr(III) acetylacetonate ($Cr(C_5H_7O_2)_3$) (blue) in the fitting model. As Fig. 8D shows, the latter two compounds appear localized in the superficial brown alteration layer, while the lead chromate-based compound is the main constituent of the yellow paint underneath.

The LSLC fitting of a line of XANES spectra obtained perpendicular to the exposed surface of the sample (Fig. 8C) yields a similar $[Cr(III)]/[Cr_{total}]$ ratio profile for the data obtained both at P06 and ID21 (Fig. 8F and G). The fraction of Cr(III) progressively decreases from the superficial brown layer (about 40–50% within the upper 4–5 µm) toward the yellow

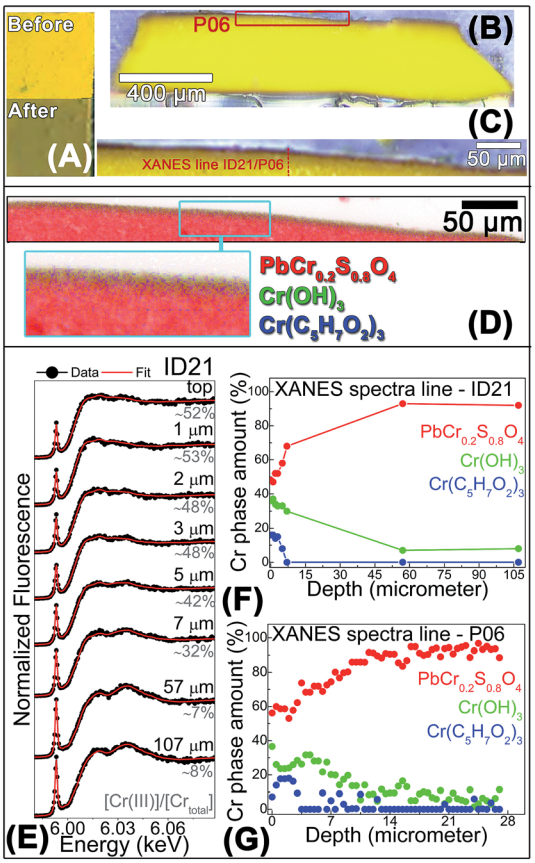

Fig. 8 (A) Photograph (top) before and (bottom) after light exposure and (B) photomicrograph of a thin section obtained from the aged $PbCr_{0.2}S_{0.8}O_4$ oil paint model. (C) Magnification of the area where the Maia 384B/P06 XANES imaging analysis was performed and (D) corresponding quantitative Cr phase maps obtained from the linear combination fitting of $PbCr_{0.2}S_{0.8}O_4$ (red), $Cr(OH)_3$ (green) and $Cr(C_5H_7O_2)_3$ (blue) of the Cr K-edge XANES stack (pixel sizes: 0.5 × 0.5 μm^2; map sizes: 460 × 40 μm^2; dwell time: 1 ms; dose: ~1.3 × 10^6 ph μm^{-2}; acquisition time: ~30 min). (E) Result of the fit (red) by linear combination of $PbCr_{0.2}S_{0.8}O_4$, $Cr(OH)_3$ and $Cr(C_5H_7O_2)_3$ to the spectra (black) obtained at ID21 (beam size ($v \times h$): 0.25 × 0.6 μm^2; dose: ~6 × 10^{11} ph μm^{-2}) and corresponding (F) percentage relative amount *vs.* the depth. (G) Equivalent results to those of (F) obtained by linear combination fitting of the single-pixel XANES spectra of the images stack collected at P06. The acquisition region of these profiles is shown in (C).

bulk of the sample (approximately 5%). Despite differences in the absolute percentage of $Cr(OH)_3$ and $Cr(C_5H_7O_2)_3$ that result from the analysis (*e.g.*, for the "top" spectra collected at ID21 and P06 the percentage relative amount of $Cr(C_5H_7O_2)_3$ was around 16% and 7%, respectively, while those of $Cr(OH)_3$ were about 36% and 40%; *cf.* Fig. 8F and G), a recurring observation is that the latter compound only seems to be present at the very surface (top 2–3 µm).

4. Conclusions

In this work, SR based FS-XANES imaging in XRF mode using both the Maia-384A (at the XFM beamline, Australian Synchrotron) and the Maia-384B detection systems (operational at the P06 X-ray micro/nanoprobe end-station, PETRA-III, DESY) was successfully used for studying the nature and distribution of secondary Cr compounds of lead chromate-based pigments (chrome yellows) and quantitatively determining their abundance in two paint micro-samples taken from artworks by Vincent van Gogh and in an artificially aged paint model. A comparison with complementary Cr K-edge µ-XRF mapping/single-point µ-XANES investigations using a more conventional SDD (operational at the ID21 microscope, ESRF) allowed us to draw the following conclusions:

(i) From a technical point of view, the XRF scanning times and the delivered X-ray doses to samples using the Maia detector could be reduced by 2–3 orders of magnitude relative to similar experiments conducted by means of a SDD. The lower spectral energy resolution of the Maia detector (290 and 375 eV) with respect to the SDD (ranging from 150 to 170 eV) did not turn out to be a limiting factor, even in the case of Ba L-lines overlapping with Cr K-lines. On the other hand, the lower spatial resolution of the Maia 384-based beamlines did not reveal at the same level of definition details of dimensions of a few micrometers that, in contrast, are clearly visible in the corresponding high-resolution maps collected using the SDD/ID21 microprobe system. However, the improved spatial and energy resolution of the Maia-384B/P06 microprobe system (~0.6 µm) with respect to that of the Maia-384A/XFM set-up (~2 µm) was successfully exploited for characterizing the composition of the superficial micrometric Cr(III)-rich alteration layer of a photochemically aged $PbCr_{0.2}S_{0.8}O_4$ paint.

(ii) Through the investigations of larger areas of the sample and the extraction of XANES profiles from all locations in the examined region, XANES imaging using Maia contributed to deepening knowledge of the nature and distribution of secondary Cr compounds relative to µ-XRF mapping/single-point µ-XANES investigations of a selection of smaller regions of interest. In all the original paint micro-samples investigated here, the widespread distribution at the paint surface of Cr(III) compounds (*i.e.*, Cr(III) sulfates and $Cr(OH)_3$) in forms of both micro-grains and micrometric layers (about 8–10 µm in thickness) strongly supports the hypothesis that they were not originally present but are products of the degradation of the original pigment.

(iii) With the exception of a few cases in which differences in the amount of Cr(III) could be ascribed to a difference in the spatial resolution and experimental set-up geometry of the microprobe systems employed, the comparable quantitative Cr-speciation results obtained by comparing the FS-XANES imaging and single-point µ-XANES data prove that the former technique may be used as a reliable method for quantitatively determining the abundance of different Cr species.

On the basis of this study, the use of large-area FS-XANES mapping using the Maia detector as complementary tool to high spatial and spectral energy resolution µ-XRF mapping/single-point µ-XANES measurements using more traditional ED-XRF detectors opens up the possibility to extend this methodological approach also to the investigation of the alteration process of other pigments.

Alternative data collection strategies relevant to explore are full-field XANES imaging (*i.e.*, not involving sample scanning) in transmission and in fluorescence mode. The former mode of operation is currently used at Stanford Synchrotron Radiation Lightsource[58] and at ID21,[59] and has found only a few applications in the field of cultural heritage, such as model paints[59] and ceramics;[60] the latter mode of operation was recently implemented at BM26 of ESRF and successfully employed for the investigation of soils.[61]

Acknowledgements

This research was supported by the Interuniversity Attraction Poles Programme – Belgian Science Policy (S2-ART project S4DA), GOA "SOLARPAINT" (Research Fund University of Antwerp, Belgium) and FWO (Brussels, Belgium) project no. G.0C12.13, G.0704.08 and G.01769.09. Support from the Italian projects PRIN (SICH Sustainability in Cultural Heritage: from diagnosis to the development of innovative system for consolidation, cleaning and protection) and PON (ITACHA Italian advanced technologies for cultural heritage applications) is also acknowledged. For the grants received thanks are expressed to ESRF (experiments EC-799, EC-1051) and DESY (experiment H-20000043). Part of this research was undertaken at the XFM beamline at the Australian Synchrotron, Victoria, Australia (experiment M4604). LM acknowledges the CNR for the financial support received in the framework of the Short Term Mobility Programme 2013. Thanks are expressed to Ella Hendriks (Van Gogh Museum, Amsterdam), Muriel Geldof (Cultural Heritage Agency of The Netherlands) and Margje Leeuwestein (Kröller-Müller Museum, Otterlo) for selecting and sharing the information on the cross-section taken from the paintings *The Bedroom* and *Falling Leaves* (*Les Alyscamps*). All the staff of the Van Gogh Museum and the Kröller-Müller Museum are acknowledged for their agreeable cooperation.

Notes and references

1 L. Bertrand, L. Robinet, M. Thoury, K. Janssens, S. X. Cohen and S. Schöder, *Appl. Phys. A: Mater. Sci. Process.*, 2012, **106**, 377–396.
2 K. Janssens, M. Alfeld, G. Van der Snickt, W. De Nolf, F. Vanmeert, M. Radepont, L. Monico, J. Dik, M. Cotte, G. Falkenberg, C. Miliani and B. G. Brunetti, *Annu. Rev. Anal. Chem.*, 2013, **6**, 399–425.
3 M. Cotte, J. Susini, J. Dik and K. Janssens, *Acc. Chem. Res.*, 2010, **43**, 705–714.
4 M. Radepont, W. De Nolf, K. Janssens, G. Van der Snickt, Y. Coquinot, L. Klaassen, M. Cotte, J. Susini, N. Metrich, A. Moscato, C. Gratziu, A. Bertagnini and M. Pagano, *J. Anal. At. Spectrom.*, 2011, **26**, 959–968.
5 M. Radepont, W. De Nolf, K. Janssens, G. Van der Snickt, Y. Coquinot, L. Klaassen and M. Cotte, *J. Anal. At. Spectrom.*, 2011, **26**, 959–968.
6 L. Robinet, M. Spring, S. Pagès-Camagna, D. Vantelon and N. Trcera, *Anal. Chem.*, 2011, **83**, 5145–5152.
7 I. Cianchetta, I. Colantoni, F. Talarico, F. D'Acapito, A. Trapananti, C. Maurizio, S. Fantacci and I. Davoli, *J. Anal. At. Spectrom.*, 2012, **27**, 1941–1948.
8 L. Samain, F. Grandjean, G. J. Long, P. Martinetto, P. Bordet, J. Sanyova and D. Strivay, *J. Synchrotron Radiat.*, 2013, **20**, 460–473.
9 L. Samain, G. Silversmit, J. Sanyova, B. Vekemans, H. Salomon, B. Gilbert, F. Grandjean, G. J. Long, R. P. Hermann, L. Vincze and D. Strivay, *J. Anal. At. Spectrom.*, 2011, **26**, 930–941.
10 L. Cartechini, C. Miliani, B. G. Brunetti, A. Sgamellotti, C. Altavilla, E. Ciliberto and F. D'Acapito, *Appl. Phys. A: Mater. Sci. Process.*, 2008, **92**, 243–250.
11 C. Santoro, K. Zarkout, A. Le Ho, F. Mirambet, D. Gourier, L. Binet, S. Pagès-Camagna, S. Reguer, S. Mirabaud, Y. Le Du, P. Griesmar, N. Lubin-Germain and M. Menu, *Appl. Phys. A: Mater. Sci. Process.*, 2014, **114**, 637–645.
12 G. Van der Snickt, J. Dik, M. Cotte, K. Janssens, J. Jaroszewicz, W. De Nolf, J. Groenewegen and L. van der Loeff, *Anal. Chem.*, 2009, **81**, 2600–2610.
13 G. Van der Snickt, K. Janssens, J. Dik, W. De Nolf, F. Vanmeert, J. Jaroszewicz, M. Cotte, G. Falkenberg and L. van der Loeff, *Anal. Chem.*, 2012, **84**, 10221–10228.
14 J. L. Mass, R. Opila, B. Buckley, M. Cotte, J. Church and A. Mehta, *Appl. Phys. A: Mater. Sci. Process.*, 2013, **111**, 59–68.
15 L. Zanella, F. Casadio, K. A. Gray, R. Warta, Q. Ma and J. F. Gaillard, *J. Anal. At. Spectrom.*, 2011, **26**, 1090–1097.
16 L. Monico, G. Van der Snickt, K. Janssens, W. De Nolf, C. Miliani, J. Dik, M. Radepont, E. Hendriks, M. Geldof and M. Cotte, *Anal. Chem.*, 2011, **83**, 1224–1231.
17 L. Monico, K. Janssens, F. Vanmeert, M. Cotte, B. G. Brunetti, G. Van der Snickt, M. Leeuwestein, J. Salvant Plisson, M. Menu and C. Miliani, *Anal. Chem.*, 2014, **86**, 10804–10811.
18 L. Monico, G. Van der Snickt, K. Janssens, W. De Nolf, C. Miliani, J. Verbeeck, H. Tian, H. Tan, J. Dik, M. Radepont and M. Cotte, *Anal. Chem.*, 2011, **83**, 1214–1223.
19 L. Monico, K. Janssens, C. Miliani, G. Van der Snickt, B. G. Brunetti, M. Cestelli Guidi, M. Radepont and M. Cotte, *Anal. Chem.*, 2013, **85**, 860–867.
20 C. Strohm, F. Perrin, M. C. Dominguez, J. Headspith, P. Linden and O. Mathon, *J. Synchrotron Radiat.*, 2011, **18**, 224–228.
21 A. J. Dent, G. Cibin, S. Ramos, S. A. Parry, D. Gianolio, A. D. Smith and P. E. Robbins, *J. Phys.: Conf. Ser.*, 2013, **430**, 012023.
22 P. Lechner, A. Pahlke and H. Soltau, *X-Ray Spectrom.*, 2004, **33**, 256–261.
23 P. Sangsingkeow, K. D. Berry, E. J. Dumas, T. W. Raudorf and T. A. Underwood, *Nucl. Instrum. Methods Phys. Res., Sect. A*, 2003, **505**, 183–186.
24 M. Cotte, J. Szlachetko, S. Lahlil, M. Salomé, V. A. Solé, I. Biron and J. Susini, *J. Anal. At. Spectrom.*, 2011, **26**, 1051–1059.

25 L. Bertrand, S. Schoeder, D. Anglos, M. Breese, K. Janssens, M. Moini and A. Simon, *Trends Anal. Chem.*, 2014, DOI: 10.1016/j.trac.2014.10.005.
26 C. G. Ryan, D. P. Siddons, R. Kirkham, Z. Y. Li, M. D. de Jonge, D. J. Paterson, A. Kuczewski, D. L. Howard, P. A. Dunn, G. Falkenberg, U. Boesenberg, G. De Geronimo, L. A. Fisher, A. Halfpenny, M. J. Lintern, E. Lombi, K. A. Dyl, M. Jensen, G. F. Moorhead, J. S. Cleverley, R. M. Hough, B. Godel, S. J. Barnes, S. A. James, K. M. Spiers, M. Alfeld, G. Wellenreuther, Z. Vukmanovic and S. Borg, *J. Phys.: Conf. Ser.*, 2014, **499**, 012002.
27 D. P. Siddons, R. Kirkham, C. G. Ryan, G. De Geronimo, A. Dragone, A. J. Kuczewski, Z. Y. Li, G. A. Carini, D. Pinelli, R. Beuttenmuller, D. Elliott, M. Pfeffer, T. A. Tyson, G. F. Moorhead and P. A. Dunn, *J. Phys.: Conf. Ser.*, 2014, **499**, 012001.
28 C. G. Ryan, R. Kirkham, R. M. Hough, G. Moorhead, D. P. Siddons, M. D. de Jonge, D. J. Paterson, G. De Geronimo, D. L. Howard and J. S. Cleverley, *Nucl. Instrum. Methods Phys. Res., Sect. A*, 2010, **619**, 37–43.
29 C. G. Ryan, *Int. J. Imag. Syst. Tech.*, 2000, **11**, 219–230.
30 E. Lombi, M. D. de Jonge, E. Donner, C. G. Ryan and D. Paterson, *Anal. Bioanal. Chem.*, 2011, **400**, 1637–1644.
31 E. Donner, D. L. Howard, M. D. de Jonge, D. Paterson, M. H. Cheah, R. Naidu and E. Lombi, *Environ. Sci. Technol.*, 2011, **45**, 7249–7257.
32 P. Wang, N. W. Menzies, E. Lombi, B. A. McKenna, M. D. de Jonge, E. Donner, F. P. C. Blamey, C. G. Ryan, D. J. Paterson, D. L. Howard, S. A. James and P. M. Kopittke, *Sci. Total Environ.*, 2013, **463**, 131–139.
33 M. Lintern, R. Anand, C. G. Ryan and D. Paterson, *Nat. Commun.*, 2013, **4**, 2274.
34 S. A. James, D. E. Myers, M. D. de Jonge, S. Vogt, C. G. Ryan, B. A. Sexton, P. Hoobin, D. Paterson, D. L. Howard, S. C. Mayo, M. Altissimo, G. F. Moorhead and S. W. Wilkins, *Anal. Bioanal. Chem.*, 2011, **401**, 853–864.
35 E. Lombi, E. Smith, T. H. Hansen, D. Paterson, M. D. de Jonge, D. L. Howard, D. P. Persson, S. Husted, C. G. Ryan and J. K. Schjoerring, *J. Exp. Bot.*, 2011, **62**, 273–282.
36 J. Z. Zhang, N. S. Bryce, R. Siegele, E. A. Carter, D. Paterson, M. D. de Jonge, D. L. Howard, C. G. Ryan and T. W. Hambley, *Integr. Biol.*, 2012, **4**, 1072–1080.
37 L. Tianqing, I. Kempson, M. D. de Jonge, D. L. Howard and B. Thierry, *Nanoscale*, 2014, **6**, 9774–9782.
38 D. L. Howard, M. D. de Jonge, D. Lau, D. Hay, M. Varcoe-Cocks, C. G. Ryan, R. Kirkham, G. F. Moorhead, D. Paterson and D. Thurrowgood, *Anal. Chem.*, 2012, **84**, 3278–3286.
39 E. Lombi, M. D. de Jonge, E. Donner, P. M. Kopittke, D. L. Howard, R. Kirkham, C. G. Ryan and D. Paterson, *PLoS One*, 2011, **6**, e20626.
40 P. M. Kopittke, M. D. de Jonge, N. W. Menzies, P. Wang, E. Donner, B. A. McKenna, D. Paterson, D. L. Howard and E. Lombi, *Plant Physiol.*, 2012, **159**, 1149–1158.
41 A. Carey, E. Lombi, E. Donner, M. D. de Jonge, T. Punshon, B. P. Jackson, M. L. Guerinot, A. H. Price and A. A. Meharg, *Anal. Bioanal. Chem.*, 2012, **402**, 3275–3286.
42 B. E. Etschmann, C. G. Ryan, J. Brugger, R. Kirkham, R. M. Hough, G. F. Moorhead, D. P. Siddons, G. De Geronimo, A. Kuczewski, P. Dunn, D. Paterson, M. D. de Jonge, D. L. Howard, P. Davey and M. Jensen, *Am. Mineral.*, 2010, **95**, 884–887.
43 B. E. Etschmann, E. Donner, J. Brugger, D. L. Howard, M. D. de Jonge, D. Paterson, R. Naidu, K. G. Scheckel, C. G. Ryan and E. Lombi, *Environ. Chem.*, 2014, **11**, 341–350.
44 P. M. Kopittke, M. D. de Jonge, P. Wang, B. A. McKenna, E. Lombi, D. Paterson, D. L. Howard, S. A. James, K. M. Spiers, C. G. Ryan, A. A. T. Johnson and N. W. Menzies, *New Phytol.*, 2014, **201**, 1251–1262.
45 C. M. Weekley, A. Shanu, J. B. Aitken, S. Vogt, P. K. Witting and H. H. Harris, *Metallomics*, 2014, **6**, 1602–1615.
46 L. Monico, K. Janssens, C. Miliani, B. G. Brunetti, M. Vagnini, F. Vanmeert, G. Falkenberg, A. Abakumov, Y. Lu, H. Tian, J. Verbeeck, M. Radepont, M. Cotte, E. Hendriks, M. Geldof, L. van der Loeff, J. Salvant and M. Menu, *Anal. Chem.*, 2013, **85**, 851–859.
47 L. Monico, K. Janssens, E. Hendriks, B. G. Brunetti and C. Miliani, *J. Raman Spectrosc.*, 2014, **45**, 1034–1045.
48 M. Salomé, M. Cotte, R. Baker, R. Barrett, N. Benseny-Cases, G. Berruyer, D. Bugnazet, H. Castillo-Michel, C. Cornu, B. Fayard, E. Gagliardini, R. Hino, J. Morse, E. Papillon, E. Pouyet, C. Rivard, V. A. Solé, J. Susini and G. Veronesi, *J. Phys.: Conf. Ser.*, 2013, **425**, 182004.
49 D. Paterson, M. D. de Jonge, D. L. Howard, W. Lewis, J. McKinlay, A. Starritt, M. Kusel, C. G. Ryan, R. Kirkham, G. Moorhead and D. P. Siddons, *AIP Conf. Proc.*, 2011, **1365**, 219–222.
50 C. G. Ryan, D. R. Cousens, S. H. Sie, W. L. Griffin, G. F. Suter and E. Clayton, *Nucl. Instrum. Methods Phys. Res., Sect. B*, 1990, **47**, 55–71.
51 C. G. Ryan, D. P. Siddons, R. Kirkham, P. A. Dunn, A. Kuczewski, G. Moorhead, G. De Geronimo, D. J. Paterson, M. D. de Jonge, R. M. Hough, M. J. Lintern, D. L. Howard, P. Kappen and J. Cleverley, *AIP Conf. Proc.*, 2010, **1221**, 9–17.
52 Y. Liu, F. Meirer, P. A. Williams, J. Wang, J. C. Andrews and P. Pianetta, *J. Synchrotron Radiat.*, 2012, **19**, 281–287.
53 V. De Andrade, J. Ganne, B. Dubacq, C. G. Ryan, F. Bourdelle, A. Plunder, G. Falkenberg and J. Thieme, *J. Phys.: Conf. Ser.*, 2014, **499**, 012012.
54 V. A. Solé, E. Papillon, M. Cotte, P. Walter and J. Susini, *Spectrochim. Acta, Part B*, 2007, **62**, 63–68.
55 B. Ravel and M. Newville, *J. Synchrotron Radiat.*, 2005, **12**, 537–541.
56 E. Hendriks and M. Geldof, in *Vincent Van Gogh Paintings 2: Antwerp & Paris, 1885–1888*, ed. E. Hendriks and L. Van Tilborgh, Waanders Publishers, Amsterdam and Zwolle, 2011, pp. 90–143.

57 M. Vellekoop, M. Geldof, E. Hendriks, L. Jansen and A. de Tagle, *Van Gogh's studio practice*, Yale University Press, New Haven and London, 2013.
58 Y. Liu, J. C. Andrews, F. Meirer, A. Mehta, G. S. Carrasco, P. Sciau, Z. Mester and P. Pianetta, *AIP Conf. Proc.*, 2011, **1365**, 357–360.
59 B. Fayard, E. Pouyet, G. Berruyer, D. Bugnazet, C. Cornu, M. Cotte, V. De Andrade, F. Di Chiaro, O. Hignette, J. Kieffer, T. Martin, E. Papillon, M. Salomé and V. A. Solé, *J. Phys.: Conf. Ser.*, 2013, **425**, 192001.
60 F. Meirer, Y. Liu, E. Pouyet, B. Fayard, M. Cotte, C. Sanchez, J. C. Andrews, A. Mehta and P. Sciau, *J. Anal. At. Spectrom.*, 2013, **28**, 1870–1883.
61 P. Tack, J. Garrevoet, S. Bauters, B. Vekemans, B. Laforce, E. Van Ranst, D. Banerjee, A. Longo, W. Bras and L. Vincze, *Anal. Chem.*, 2014, **86**, 8791–8797.